

Analysis of Position Estimation Error in Signal-Injection Sensorless Control Induced by Inverter dv/dt-Based Current Measurement Noise

Yoon-Ro Lee[✉], Member, IEEE, Jiwon Yoo[✉], Member, IEEE, Inhwi Hwang[✉], Member, IEEE, and Seung-Ki Sul[✉], Fellow, IEEE

Abstract—This article discusses position estimation error in signal-injection sensorless control (SISC) induced by the current measurement noise of closed-loop Hall effect current sensor, when it is installed in an inverter system. For the first step, an equivalent circuit modeling of the current sensor in the inverter system is proposed, which includes the parasitic capacitances between the inverter and sensor. The presented modeling can explain how the high dv/dt of the inverter switching generates the leakage current through the parasitic capacitances, resulting in the measurement noise. The noise is sampled with analog to digital conversion, and it affects the rotor position estimation signal with the SISC algorithm. As a result, it is revealed that considerable position estimation error occurs from the noise. The experimental results are provided to verify the proposed theory and confirm the noise effects on the SISC performance.

Index Terms—Closed-loop Hall effect current sensor (CHCS), current measurement noise, inverter dv/dt, parasitic capacitance, position estimation error, signal-injection sensorless control (SISC).

I. INTRODUCTION

SIGNAL-INJECTION sensorless control (SISC) is a rotor position estimation technique used at a standstill and a low speeds, which is adopted to reduce the system cost and maximize the system reliability in extreme environments. This technique observes the current response from the high-frequency voltage injection and estimates the rotor position [1], [2], [3], [4], or the rotor flux information [24], [25]. The magnitude of the signal depends on the saliency of a target motor, which means L_q/L_d ratio. In the ideal and theoretical environments, such as a computer simulation or a hardware-in-the-loop system, if there exists a slight saliency, the SISC operation can track the rotor position with reasonable accuracy. However, in the actual field application, there are many disturbances that induce significant

Manuscript received 31 March 2022; revised 21 June 2022 and 27 July 2022; accepted 14 August 2022. Date of publication 29 August 2022; date of current version 10 October 2022. This work was supported by the Seoul National University Electric Power Research Institute (SEPRI). Recommended for publication by Associate Editor G. De Donato. (*Corresponding author:* Yoon-Ro Lee.)

The authors are with the Electrical and Computer Engineering, Seoul National University, Seoul 08826, South Korea (e-mail: dbfsfh92@snu.ac.kr; jiwon.yoo@epel.snu.ac.kr; snuhwi96@gmail.com; sulsk@snu.ac.kr).

Color versions of one or more figures in this article are available at <https://doi.org/10.1109/TPEL.2022.3202170>.

Digital Object Identifier 10.1109/TPEL.2022.3202170

errors in the position estimation. The disturbance factors can be divided into two kinds of factors, which are intrinsic and extrinsic to the motor's own characteristics.

The intrinsic factors are related to the physical characteristics of the target motor itself, e.g., cross-coupling inductance, magnetic saturation, and spatial harmonics. The factors are not affected by the types of the SISC method, whether the injected signal is pulsating or rotating, sinusoidal wave or square wave. Also, the intrinsic factors do not depend on the magnitude of the injected signal. As they are inevitable problems, there have been many research works that suggest in-depth analyses about the nonideal behaviors of the motor and overcome the disturbances with compensation functions or precalculated look-up tables [5], [6], [7], [8]. Also, there were some attempts with learning-based methods [9], [10].

The extrinsic factors come from the outside of the target motor. The most widely known factor is the inverter nonlinearity, i.e., the dead time effects and the forward voltage drop of semiconductors [11], [12], [13], [14], [15]. In addition, asymmetry of three-phase system [15], [16], scale error of the current sensors [17], [18], and analog to digital conversion (ADC) quantization error may also deteriorate the position estimation performance [26], [27]. A simple way to alleviate the extrinsic disturbances is increasing the injected voltage level, but it results in decreased efficiency, increased acoustic noise, and increased torque ripple. In that sense, the main applications of the SISC have been the motors with large saliency, such as interior permanent magnet synchronous motors (IPMSMs), where small injected voltage level can induce relatively large position signal. In this article, one more extrinsic disturbance factor for the SISC, which was not widely known in the field, is newly analyzed. That is the current measurement noise from the closed-loop Hall effect current sensor (CHCS), installed in the inverter system.

Most industrial drives adopt the Hall effect-based current sensors for their current measurement. They are advantageous compared to the other methods, such as voltage sensing via shunt resistor or ac transducer in aspect of galvanic isolation, dc measurement, and high accuracy. Regarding the configuration of the Hall effect-based current sensors, the closed-loop type is preferred over the open-loop type for its superior linearity of the current measurement. Although they are widely used and have many merits, the CHCSs generate undesirable noise when they are used in a high dv/dt inverter system. The high dv/dt

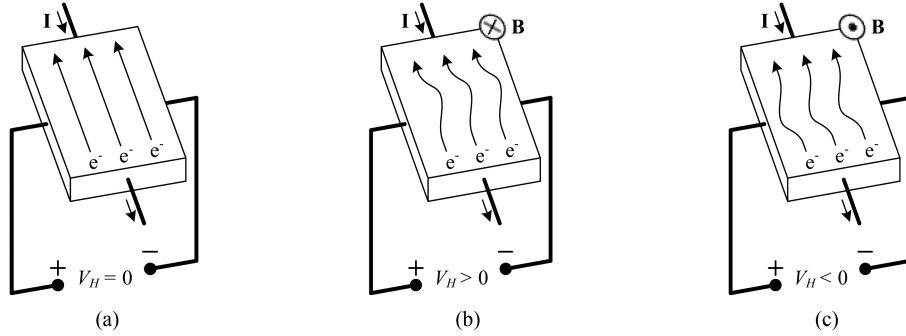


Fig. 1. Magnetic field is (a) null, (b) going into, and (c) going out of Hall effect sensor.

from fast switching of the inverter induces the leakage current flowing from the inverter to the sensor through parasitic capacitances. The leakage current results in the measurement noise. The noise level would be small enough to be ignored where the fundamental current matters, such as current regulation or overcurrent protection. However, the induced noise would affect the SISC operation, where the rotor position estimation is based on a current signal of small magnitude.

This article investigates how the noise is coupled from dv/dt of the inverter system to the CHCS. It mainly deals with the equivalent circuit modeling, including the current sensor, the inverter, and the parasitic capacitances. With the equivalent circuits, the current measurement noise from the leakage current is analyzed. The analysis is verified with various experimental results. In particular, the experiments with the sensors from the various manufacturers support the generality of the presented analysis. Furthermore, this article analyzes how the dv/dt induced noise is sampled by ADC process and how the sampled noise affects the position estimation performance in the conventional SISC algorithms [7], [8]. The proposed analysis fully considers ADC sampling effect in signal processing of SISC. The results show that the current measurement noise can be critical to the SISC performance.

II. EQUIVALENT CIRCUIT MODELING OF HALL EFFECT CURRENT SENSOR

A main part of the CHCS is the Hall effect sensor. The basic principle of the Hall effect sensor is depicted in Fig. 1 [19]. In the sensor, a constant current is flowing in the vertical direction by an external current source. The voltage induced in the horizontal direction is defined as Hall voltage, V_H . When a magnetic field is penetrating through the Hall effect sensor, V_H is induced because the electron paths are curved by Lorentz force [19], [20]. In Fig. 1(a), V_H is maintained as null since the magnetic field is absent. In (b), the magnetic field goes into the Hall sensor and V_H is induced as a positive value. In (c), the flux is going out of the Hall sensor and V_H is induced as a negative value. V_H is expressed as

$$V_H \propto \mathbf{I} \times \mathbf{B}. \quad (1)$$

\mathbf{I} in the equation is a constant current vector and \mathbf{B} is a magnetic flux density vector to the Hall effect sensor plane.

If \mathbf{B} is always orthogonal to the sensor plane, V_H is directly proportional to \mathbf{B} .

In Fig. 2(a), a typical structure of CHCSs is represented [20]. As shown in the figure, a Hall effect sensor exists in the air gap of the “C” shape core. A wire carrying the target current is going through the center of the core. When the current, I_p , flows in the wire, the magnetic field is induced in the core with Ampere's circuital law

$$\nabla \times \mathbf{H} = \mathbf{J}_f + \frac{\partial \mathbf{D}}{\partial t}. \quad (2)$$

\mathbf{H} , \mathbf{J}_f , and \mathbf{D} are vectors of magnetic field intensity, free current density, and electric flux density, respectively. Then, the magnetic field goes through the Hall effect sensor orthogonally and V_H is induced. On the other hand, N turns of enameled winding are constructed at a side of the core. N is generally designed between 1000 and 5000 turns. Current flowing in the secondary winding is defined as I_s , and one end of the winding is connected to a current regulator. The regulator drives I_s to nullify V_H by making equilibrium of the magnetic field produced by I_p and I_s . As a result, the ratio of I_p and I_s is approximately maintained as $N:1$. Because the magnetic flux in the core is extremely zero, the operating point on B–H plane remains near the origin regardless of I_p . Therefore, the accuracy and the linearity could be guaranteed by avoiding magnetic saturation of the core and hysteresis loss-based temperature variation. The other end of the N turns winding is connected to an external measurement resistor, R_{sense} , and I_s flows through R_{sense} . Then, the voltage across R_{sense} , V_{sense} , is generally converted into a digital value with ADC, and I_p could be calculated by

$$I_{p,\text{sense}} = N \cdot \frac{V_{\text{sense}}}{R_{\text{sense}}}. \quad (3)$$

In an ideal current measurement system, $I_{p,\text{sense}}$ would be identical to I_p .

The equivalent circuit of the measurement system can be depicted as Fig. 2(b). The current regulator's impulse response can be represented in the time domain as $h(t)$. With that, I_s is expressed as a convolution form as $I_s = h(t) * V_H$. Each manufacturer and each product would have a different $h(t)$. In many catalogs, the measurement bandwidth is suggested as 200 kHz.

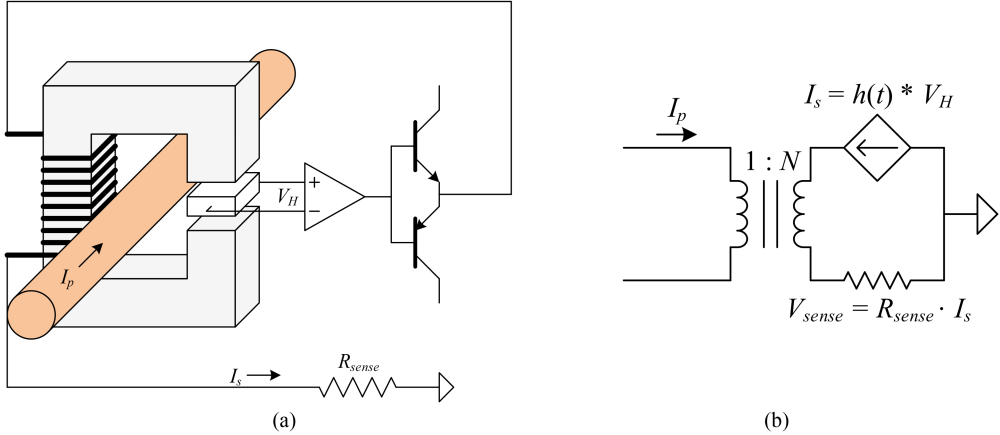


Fig. 2. (a) Typical structure. (b) Equivalent circuit of CHCSs.

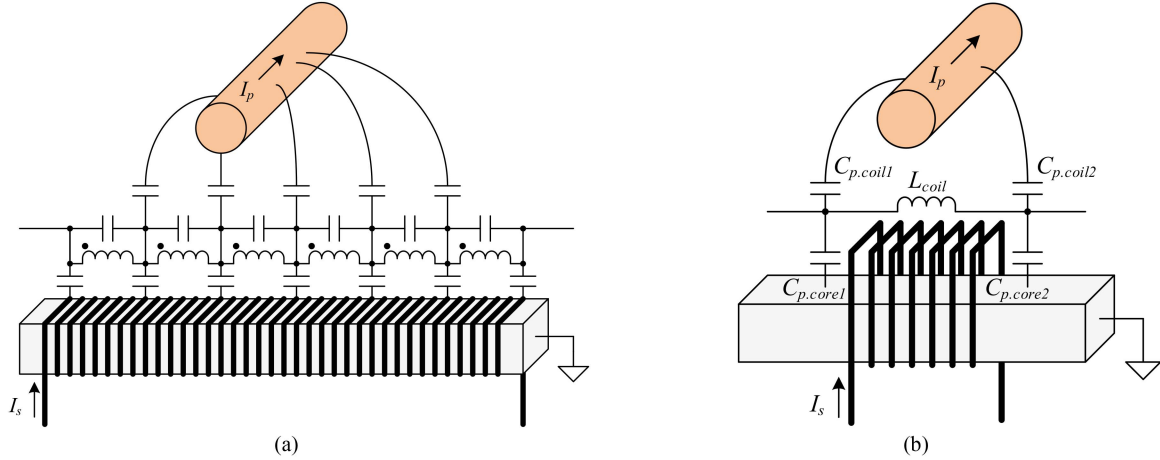


Fig. 3. (a) Parasitic capacitances in current measurement system. (b) Equivalent circuit.

III. MEASUREMENT NOISE FROM INVERTER DV/DT

There are always parasitic capacitances in the current measurement system, as depicted in Fig. 3(a). There exist capacitances between the primary wire and the secondary winding, between the winding and the core, and among the winding. It can be roughly integrated into a simple circuit, as shown in Fig. 3(b). The capacitances between the primary wire and the secondary winding are defined as $C_{p.coil1}$ and $C_{p.coil2}$. The capacitances between the winding and the core are defined as $C_{p.core1}$ and $C_{p.core2}$. C_p stands for the parasitic capacitances. The inductance of the winding is defined as L_{coil} . Since L_{coil} is proportional to the square of N , $1000 \sim 5000$, it has considerable value.

In Fig. 4(a), a current sensor is installed in the output terminal of “ x ” phase inverter leg. The equivalent circuit of the current sensor in Fig. 2(b) is adopted in the inverter system of Fig. 4(a). In the figure, V_{dc} is the dc-link voltage. In conjunction with the circuit in Fig. 3(b), the overall circuit including the inverter and the sensor can be depicted as Fig. 4(b), where two additional parasitic capacitances, $C_{p.inv}$ and $C_{p.sense}$, are introduced to express the earth-coupled parasitic capacitances of the inverter

and the sensing circuit. Note that one end of the inverter leg output is opened. Because I_p cannot flow ideally in the circuit diagram, I_s and v_{sense} are expected to be maintained as null. However, the leakage current flows through R_{sense} when the inverter is switching. Then, v_{sense} is produced and it is converted into current measurement noise.

In Fig. 4(b), the pole voltage of “ x ” phase is denoted as v_{xp} , which alternates between V_{dc} and zero. Behind the dependent current source symbol, a capacitance is shown with a dotted line as C_{cs} , which stands for the capacitors established in the dependent current source circuit. With the circuit, two steps of leakage current paths are considered as Fig. 5, and they are highlighted in red color. In Fig. 5(a), the path at the rising time of the pole voltage is represented. In Fig. 5(b), the path at the steady state after the rising time is represented. Because the rising and the falling characteristics can be considered symmetric, descriptions about the falling sequence are omitted in this article. In the figures, $C_{p.inv}$ and $C_{p.sense}$ are replaced by a short circuit, since they are series connected to $C_{p.coil1} + C_{p.coil2}$ and have much larger capacitance than $C_{p.coil1} + C_{p.coil2}$. The next chapter gives specific verifications about Fig. 5 with the experimental results.

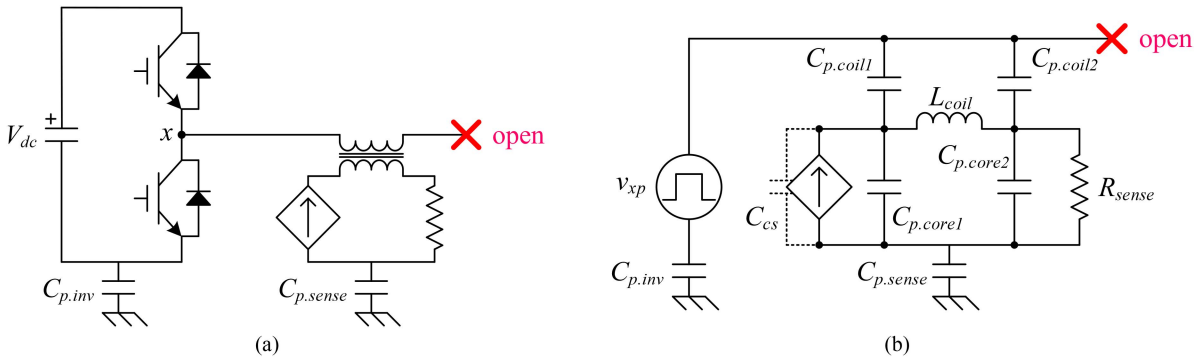


Fig. 4. (a) Inverter system with current sensor. (b) Parasitic capacitances combined circuit.

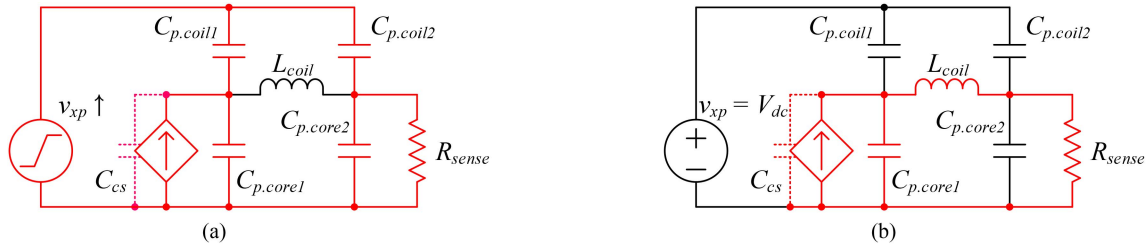


Fig. 5. Leakage current path at (a) rising time and (b) steady state.

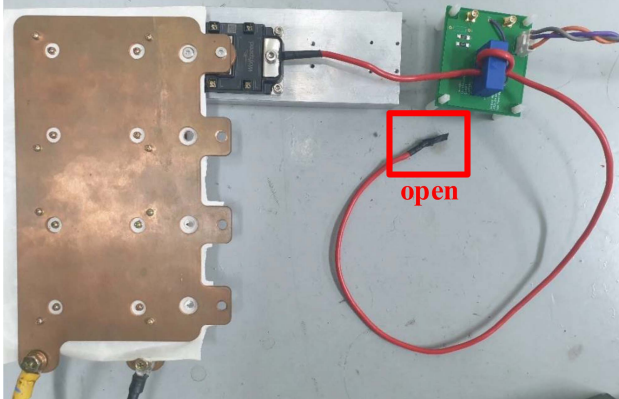


Fig. 6. Experimental set-up with a half-bridge and a current sensor.

IV. EXPERIMENTAL ANALYSIS OF NOISE-INDUCING MECHANISM

An experimental set-up with a half-bridge and a current sensor is displayed in Fig. 6. One end of a red-colored 6 mm^2 copper wire is connected to the output terminal of the half-bridge, and the other end is opened. Also, the middle of the wire goes through the center of the current sensor with two turns. The original rated current of the current sensor is $50 \text{ A}_{\text{rms}}$, but the two turns make it be a half. R_{sense} is selected as 215Ω .

In the configuration, the impedance of each circuit component is measured with an impedance analyzer and the results are depicted in Fig. 7. In normal conditions, a switching mode power supply (SMPS) is connected to the current sensor, but the SMPS is disconnected not to affect the impedance measurement. In the

measurement, the enclosure of the current sensor is removed and the impedance analyzer is directly connected to each node with a short copper wire. Under 100 kHz , L_{coil} is around 100 mH , $C_{p.core1} + C_{p.core2}$, 7.5 pF , and $C_{p.coil1} + C_{p.coil2}$, 3.7 pF . By dealing with the dependent current source as a resistor–capacitor (R–C) series equivalent circuit, the impedance analyzer measures R and C separately, as shown in Fig. 7(d). Above 30 kHz , the capacitance is about 104 pF and the resistance is between 1 and $2 \text{ k}\Omega$. However, the dependent current source circuit comprises many semiconductors, so it is hard to treat the $1 \sim 2 \text{ k}\Omega$ as a real resistance. Two additional parasitic capacitances are also measured as $C_{p.inv} = 500 \text{ nF}$ and $C_{p.sense} = 18 \text{ nF}$, enough large to be neglected. Two kinds of experiments are carried out with the experimental set-up to verify the leakage current paths, proposed in Fig. 5(a) and (b). The first experimental results are shown in Figs. 8 and 9. The second results are shown in Figs. 10 and 11. In the first/second experiments, the SMPS for the current sensor is turned-off/on.

In the first experiments, the dependent current source in the current sensor does not work and only reveals as a capacitance, C_{cs} , since the SMPS is turned-off. The voltage, v_{cs} , stands for the voltage across the dependent current source. Fig. 8 shows short-term results, which focus on the circuit behavior at the rising time corresponding to Fig. 5(a). Fig. 9 shows long-term results, which focus on the steady state corresponding to Fig. 5(b).

In the experiments, the gate resistors have been changed to four different values to see the effect of dv/dt of the pole voltage at the rising time. The dv/dt variation can be observed in v_{xp} graphs in Fig. 8. Since the dependent current source is deactivated by turning off SMPS, each relationship between the voltages of Fig. 5(a) can be expressed as simple equations as

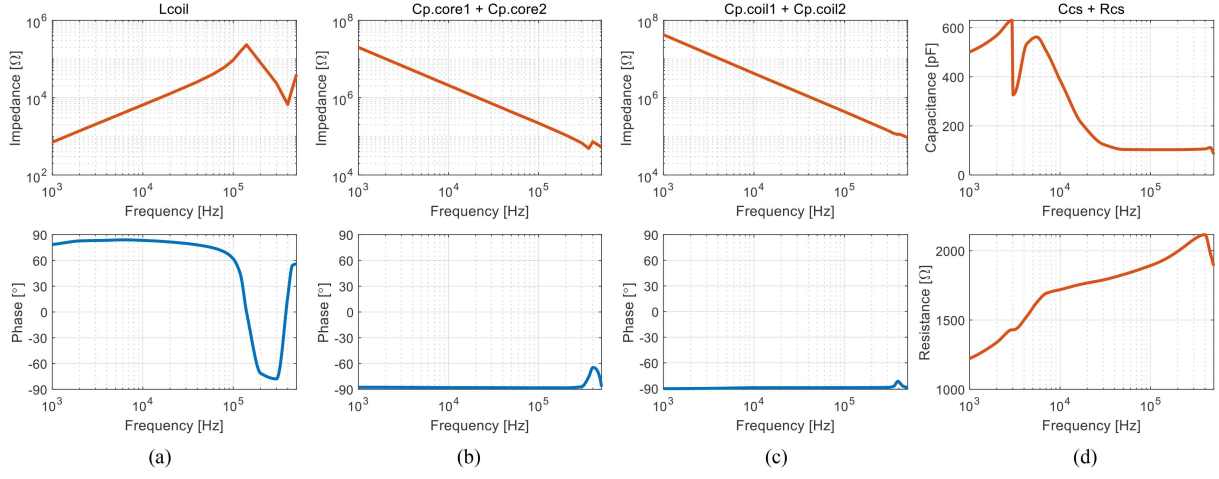


Fig. 7. Measured results with impedance analyzer. (a) L_{coil} . (b) $C_{p.\text{core}1} + C_{p.\text{core}2}$. (c) $C_{p.\text{coil}1} + C_{p.\text{coil}2}$. (d) $C_{\text{cs}} + R_{\text{cs}}$.

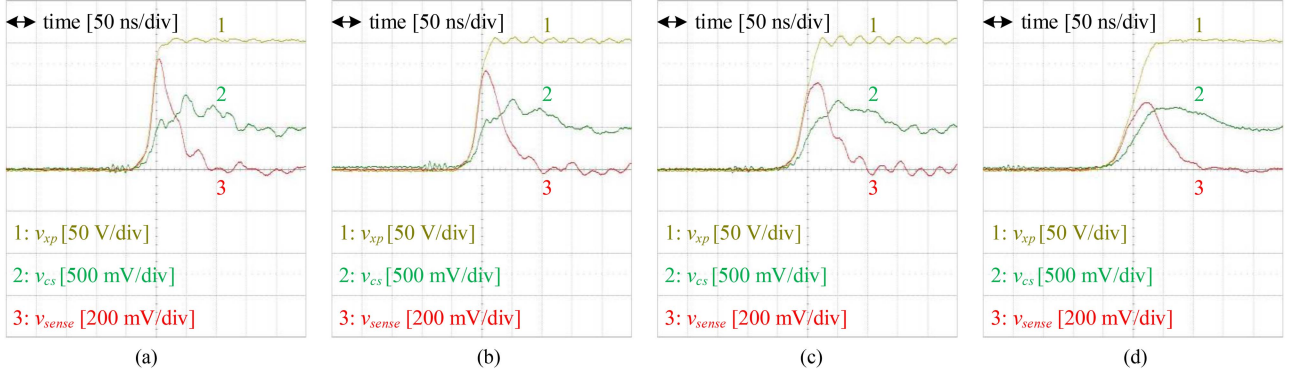


Fig. 8. Voltage signals induced by dv/dt of pole voltage. Short-term results with turned-off SMPS. Gate resistor = (a) 2.2Ω , (b) 3Ω , (c) 5Ω , and (d) 10Ω .

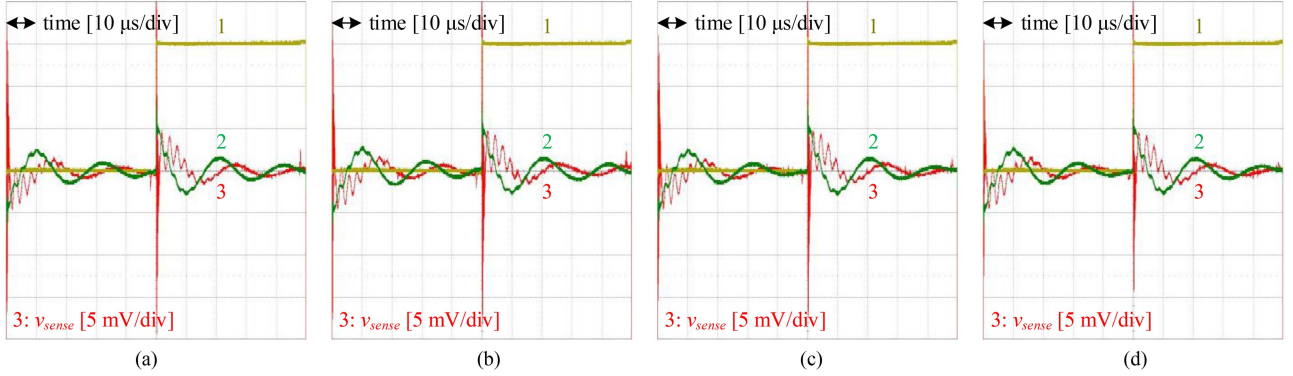


Fig. 9. Voltage signals induced by dv/dt of pole voltage. Long-term results with turned-off SMPS. Gate resistor = (a) 2.2Ω , (b) 3Ω , (c) 5Ω , and (d) 10Ω .

follows:

$$\frac{V_{\text{cs}}(s)}{V_{\text{xp}}(s)} = \frac{C_{p.\text{coil}1}}{C_{p.\text{coil}1} + C_{p.\text{core}1} + C_{\text{cs}}} \quad (4)$$

$$\frac{V_{\text{sense}}(s)}{V_{\text{xp}}(s)} = \underbrace{sR_{\text{sense}}C_{p.\text{coil}2}}_{\text{Differentiator}} \cdot \underbrace{\frac{1}{1 + sR_{\text{sense}}(C_{p.\text{coil}2} + C_{p.\text{core}2})}}_{\text{LPF}} \quad (5)$$

In (4), the relationship between v_{xp} and v_{cs} is expressed as the ratio of the capacitances. v_{cs} right after the rising time has very similar values in all four cases of Fig. 8(a)–(d), approximately 720 mV, because the final value of each v_{xp} is V_{dc} , 150 V, regardless of the individual dv/dt . In the denominator of (4), C_{cs} is the dominant component, as measured in Fig. 7. So the equation can be approximated as a simple ratio as $C_{p.\text{coil}1}/C_{\text{cs}}$. By adopting C_{cs} in the ratio as the measured value, 104 pF, $C_{p.\text{coil}1}$ can be calculated as $720 \text{ mV}/150 \text{ V} \times 104 \text{ pF} = 0.5 \text{ pF}$.

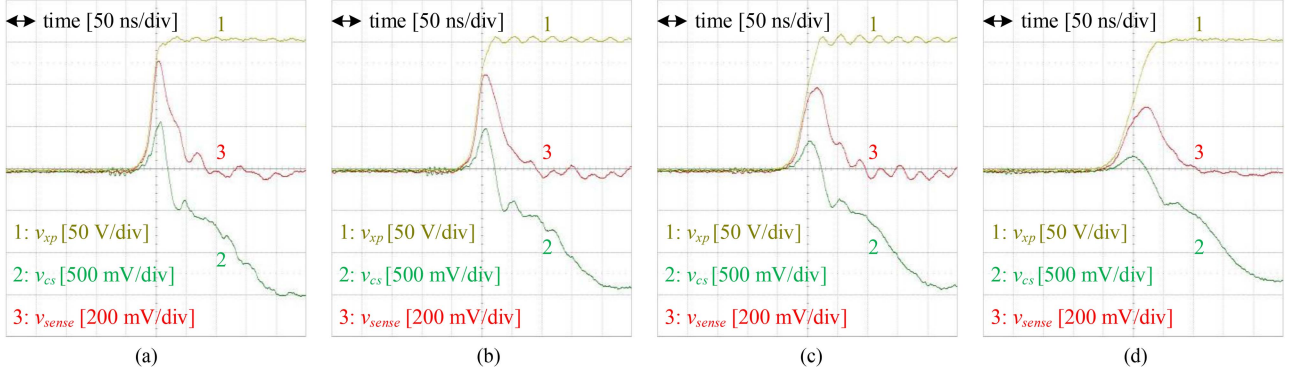


Fig. 10. Voltage signals induced by dv/dt of pole voltage. Short-term results with turned-on SMPS. Gate resistor = (a) $2.2\ \Omega$, (b) $3\ \Omega$, (c) $5\ \Omega$, and (d) $10\ \Omega$.

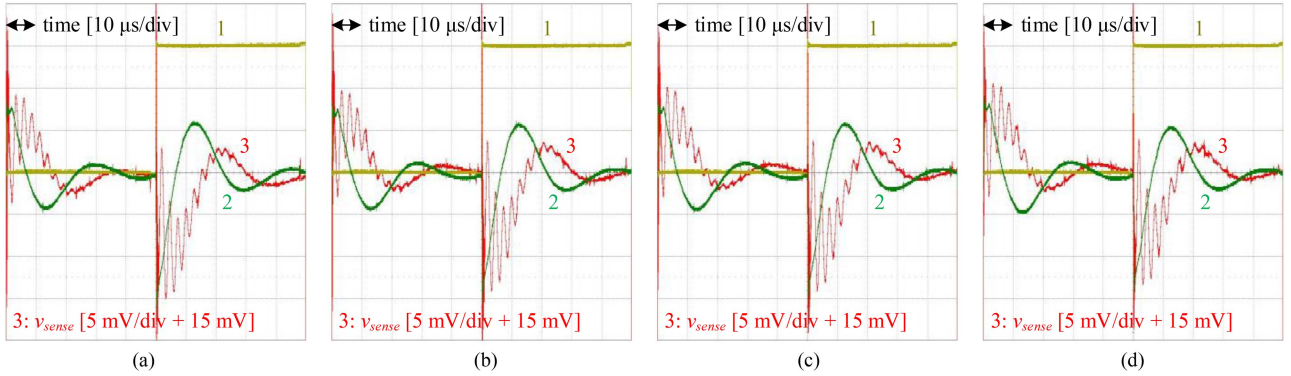


Fig. 11. Voltage signals induced by dv/dt of pole voltage. Long-term results with turned-on SMPS. Gate resistor = (a) $2.2\ \Omega$, (b) $3\ \Omega$, (c) $5\ \Omega$, and (d) $10\ \Omega$.

In (5), the relationship between v_{xp} and v_{sense} in Laplace domain is expressed as a multiplication of a differentiator and a low pass filter (LPF). Therefore, as the slope of v_{xp} decreases, the maximum value of v_{sense} also decreases, as shown in Fig. 8. When v_{xp} settles to V_{dc} after the rising time, v_{sense} becomes null thanks to the differentiator. Then, $R_{sense}C_{p.coil2}$ in (5) can be roughly calculated with v_{xp} and v_{sense} waveforms of Fig. 8, by dividing the maximum value of v_{sense} with the maximum slope of v_{xp} . Because R_{sense} is selected as $215\ \Omega$, $C_{p.coil2}$ is calculated as $0.62\ pF$.

After the analysis focusing on the rising time, long-term results are represented in Fig. 9. The vertical scales of v_{xp} and v_{cs} are the same as Fig. 8, while that of v_{sense} becomes smaller from 200 to 5 mV per one division. As aforementioned, the leakage current path in the steady state follows the route in Fig. 5(b). In the configuration, $C_{p.core2}$, which is parallel connected to R_{sense} , has a much larger impedance than R_{sense} under several mega-Hertz. So $C_{p.core2}$ can be excluded from the leakage path. Even the dependent current source was deactivated. As a result, the path operates as a simple series-connected resistor—inductor–capacitor (R-L-C) resonant circuit. The R corresponds to R_{sense} , L to L_{coil} , and C to $C_{cs} + C_{p.core1}$. In the typical R-L-C circuit, the differentiation of the voltage across the C component is proportional to the voltage across the R component. It exactly matches the relationship between the waveforms of v_{sense} and v_{cs} , as shown in Fig. 9. In the figure, four cases have similar waveforms regardless of the resistances of the gate resistors,

TABLE I
CAPACITANCE VALUES OBTAINED BY TWO DIFFERENT METHODS

Measured value (impedance analyzer)		Calculated value (experimental results)	
$C_{p.coil1} + C_{p.coil2}$	$3.7\ pF$ ($< 100\ kHz$)	$C_{p.coil1}$	$0.5\ pF$
$C_{p.core1} + C_{p.core2}$	$7.5\ pF$ ($< 100\ kHz$)	$C_{p.coil2}$	$1.12\ pF$
C_{cs}	$104\ pF$ ($> 30\ kHz$)	$C_{cs} + C_{p.core1}$	$118.42\ pF$

because the initial condition of the resonance is maintained as the same as $v_{cs} = 720\ mV$ and $v_{sense} = 0\ mV$. Then, the resonant frequency of the R-L-C circuit can be expressed as

$$f_{res} = \frac{1}{2\pi\sqrt{L_{coil}(C_{cs} + C_{p.core1})}}. \quad (6)$$

The resonant frequency in the figure is revealed as $46.25\ kHz$. By adopting L_{coil} in (6) as $100\ mH$, as measured in Fig. 7(a), $C_{cs} + C_{p.core1}$ is calculated as $118.42\ pF$.

The values experimentally obtained so far are summarized in the right two columns of Table I, while the measured values in Fig. 7 are rewritten in the left two columns for comparison purposes. As shown in the table, $C_{p.coil1} + C_{p.coil2}$ was measured

TABLE II
MOTOR AND INVERTER SPECIFICATIONS

L_{ds}	7.13 mH	V_{dc}	150 V
L_{qs}	11.04 mH	F_{sw}	10 kHz
L_{dqs}	0 mH	T_s	5 μ s
λ_f	62.5 mWb·t	$F_s = I/T_s$	20 kHz
R_s	0.8 Ω	V_{inj}	20 V
$I_{s.Rated}$	4.08 A _{pk}	F_{inj}	5 kHz

as 3.7 pF under 100 kHz, but the experimental results give the value as 1.12 pF. During the experiments in Fig. 8, v_{xp} can be expressed as (7) in the Laplace domain, while T_r stands for the rising time

$$V_{xp}(s) = V_{dc} \cdot \frac{1}{T_r s^2} \cdot (1 - e^{-T_r s}). \quad (7)$$

Since the frequency spectrum is located over the impedance measurement range, the measured impedances could differ in the unmeasured high-frequency range. It can be seen in Fig. 7(b) and (c) that the capacitances are already reduced beyond 400 kHz. Although there is a difference between the measured and the experimentally obtained values, the orders are the same. Therefore, it can be said that the proposed modeling would be applicable to guess the leakage current.

On the other hand, $C_{cs} + C_{p.core1}$ was obtained as 118.42 pF from the experiment in Fig. 9. During the experiment, the resonance frequency is measured as 46.25 kHz, which is in the frequency range of the impedance analyzer. It can be noticed that $C_{cs} + C_{p.core1}$ calculated in the experiments is similar to the values of C_{cs} and $C_{p.core1} + C_{p.core2}$ measured by the impedance analyzer. Consequently, it can be said that the leakage current paths of Fig. 5 are verified.

For the next step, the same experiments are implemented with the turned-on SMPS, which means the dependent current source is activated. Fig. 10 shows short-term results, which focus on the rising time corresponding to Fig. 5(a). Fig. 11 shows long-term results, which focus on the steady state corresponding to Fig. 5(b).

In Fig. 10, each v_{sense} waveform is very similar to the corresponding waveform in Fig. 8. It can be explained with Fig. 5(a) that the leakage current path through R_{sense} is separated with the path through the dependent current source. On the other hand, the waveforms of v_{cs} are changed because the dependent current source reacts to the leakage current. However, v_{cs} right after the rising time has very similar values in all four cases, so the initial condition of resonance is maintained as the same level. Therefore, the resonance is expected to be taken place in the same tendency, regardless of the gate resistor variation.

In Fig. 11(a)–(d), long-term waveforms of v_{cs} and v_{sense} in four cases are very similar. There exists a default value of –15 mV in v_{sense} , so v_{sense} graphs are center aligned with 15 mV offset. In the ADC process, the default value is premeasured, saved in the memory, and subtracted from the measured v_{sense} .

In Fig. 11(a)–(d), the waveforms are different from Fig. 9(a) to (d), especially the resonant frequency reduced from 46.25 to 33 kHz. For the detailed analysis on the reduction, $h(t)$ of the dependent current source should be figured out, but it would vary according to manufacturers and products, and it is hard to identify $h(t)$ quantitatively. One end of the red-colored copper wire is opened in the experiments. Therefore, when v_{sense} of Fig. 11 is converted into a digital signal with ADC and changed into I_p by (3), it can be thought that the measured I_p is a pure measurement noise. The ADC results of Fig. 11 are denoted as $i_{xs \cdot noise}$, which means “x” phase current measurement noise, and represented in Fig. 12. The obtention process of Fig. 12 is described in the following paragraph.

The sampling process of the ADC generally occurs at the peak and the valley of the triangle carrier wave of PWM [21]. In the process, the current measurement noise is sampled together with the real current. The noise component of v_{sense} is induced by the high dv/dt which is generated at the switching instant, as shown in Figs. 8–11, and it is a very important point that the time interval between the switching instant and the sampling instant can be adjusted by the pole voltage reference, v_{xp}^* . In other words, when v_{xp}^* changes, v_{sense} waveform is time shifted in the sampling period, and the value of v_{sense} at the sampling instant varies. Therefore, the current measurement noise can be expressed as a function of v_{xp}^* between $-V_{dc}/2$ and $V_{dc}/2$, in on/off-sequence separately, as shown in Fig. 12. The noise waveforms of the graphs in on/off-sequence are origin symmetry. Every point on the graphs is placed with 1 V interval. Also, each graph has been averaged by 500 times repeated sampling results. Each dotted circle part of Fig. 12 is denoted as “impulse part,” and the remaining part is denoted as “resonance part.” The impulse part corresponds to the impulse signal of v_{sense} in Fig. 10. Therefore, the impulse part was expected to be generated when v_{xp}^* equals to $-V_{dc}/2$ and $V_{dc}/2$ in on- and off-sequence, respectively, where the switching instant coincides with the sampling instant. However, as shown in Fig. 12, the impulse part is generated when v_{xp}^* is close to –70 and 70 V in on- and off-sequence, respectively. It comes from the dead time and propagation delay of the inverter system, which delays the switching instant from the desired switching time point.

In Fig. 10, the impulse magnitude of v_{sense} varies according to the gate resistance, while the impulse part of $i_{xs \cdot noise}$ is calculated in the same level, as shown in Fig. 12. The reason is the existence of an LPF at the input of the ADC circuit. The LPF is built with a first order resistor–capacitor (R-C) circuit, whose bandwidth is designed as 400 kHz. The shapes of the resonance part of $i_{xs \cdot noise}$ in Fig. 12(a)–(d) resemble to the shapes of v_{sense} in Fig. 12(a)–(d). Consequently, it can be expected with the experimental results of Fig. 12 that the current measurement noise is generated in a similar level, if dv/dt of the pole voltage is high enough and the dc-link voltage is maintained as the same.

The same experiments are also implemented with the other manufacturers’ current sensors and different dc-link voltages. The rated current of the sensors is the same as 50 A_{rms}. Also, the circuit configurations are the same, e.g., gate resistor, two turns of copper wire, R_{sense} , etc. The results are represented in Figs. 13 and 14. The $i_{xs \cdot noise}$ waveforms of the sensors are

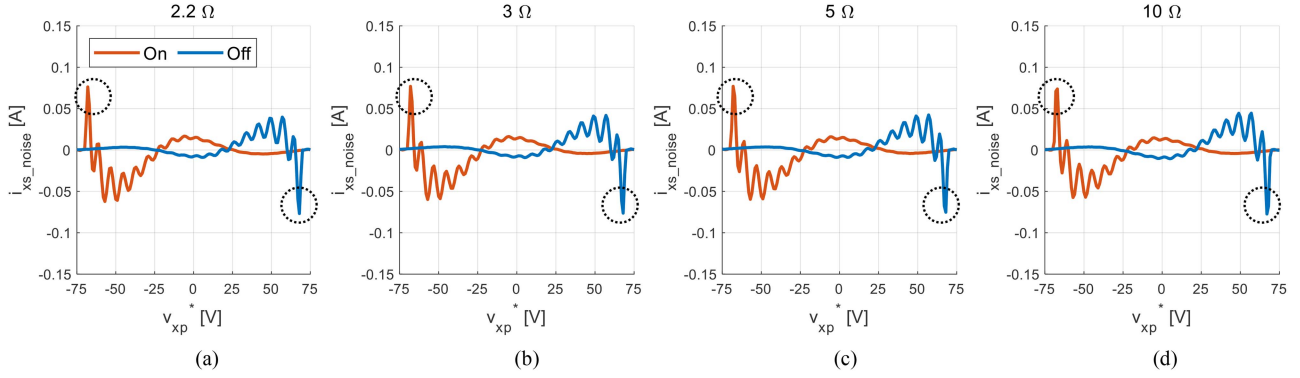


Fig. 12. ADC results of current measurement noise with four different gate resistors at $V_{dc} = 150$ V. (a) $2.2\ \Omega$. (b) $3\ \Omega$. (c) $5\ \Omega$. (d) $10\ \Omega$.

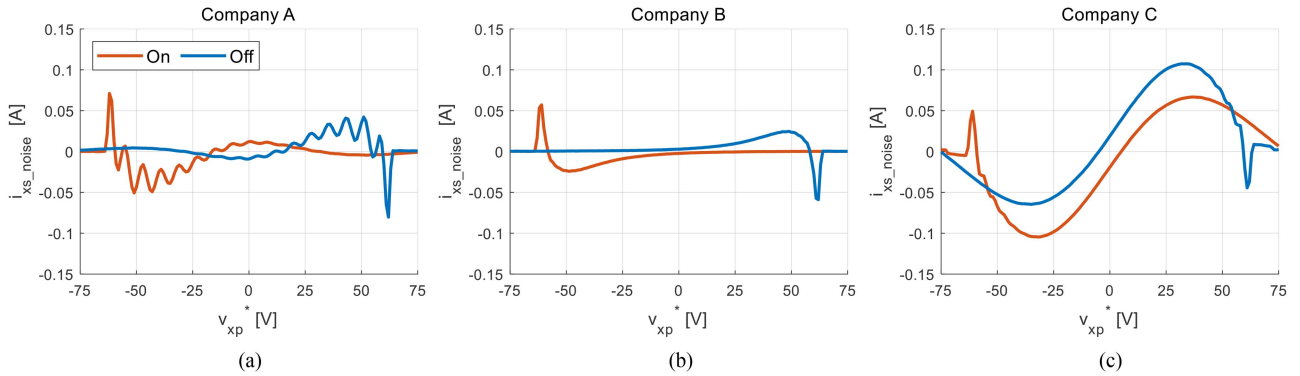


Fig. 13. ADC results of current measurement noise with three different products at $V_{dc} = 150$ V. (a) Company A. (b) Company B. (c) Company C.

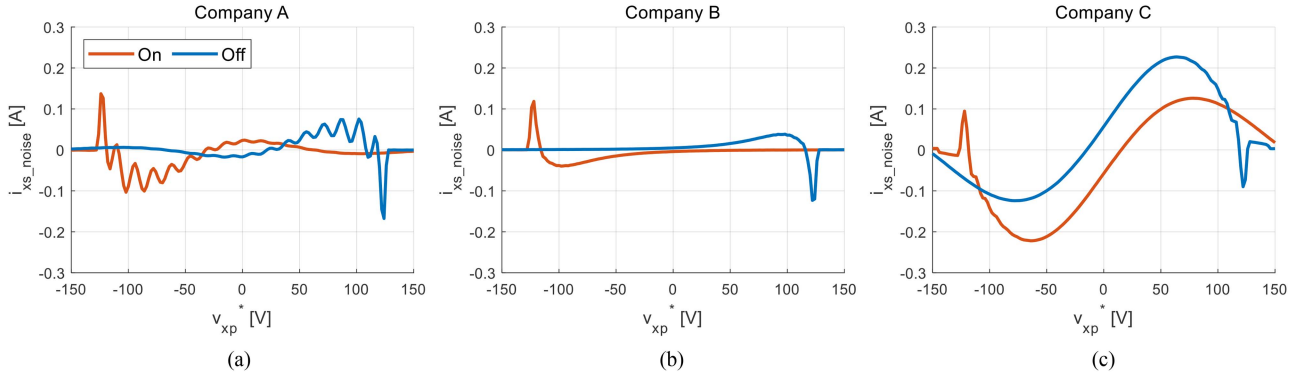


Fig. 14. ADC results of current measurement noise with three different products at $V_{dc} = 300$ V. (a) Company A. (b) Company B. (c) Company C.

different. But the two parts of i_{xs_noise} , the impulse part and the resonance part, are commonly recognized in every graph. Also, the noise level is doubled as dc-link voltage increases from 150 to 300 V. It matches the proposed noise-inducing mechanism.

V. CURRENT MEASUREMENT NOISE EFFECTS ON SIGNAL INJECTION SENSORLESS CONTROL

Detailed descriptions about the SISC can be referred in [7], [8]. Only some necessary equations are rewritten in this article and a control block diagram is redrawn in Fig. 15. The angles of rotor reference frame (RRF) and estimated rotor reference

frame (ERRF) are θ_r and $\hat{\theta}_r$, respectively. The estimation error is $\tilde{\theta}_r$ and it is defined as $\tilde{\theta}_r = \theta_r - \hat{\theta}_r$. Then, the relationship between RRF and ERRF is

$$\begin{aligned} \mathbf{x}_{dq}^{\hat{r}} &= \begin{bmatrix} x_d^{\hat{r}} \\ x_q^{\hat{r}} \end{bmatrix} = \begin{bmatrix} \cos(\tilde{\theta}_r) & -\sin(\tilde{\theta}_r) \\ \sin(\tilde{\theta}_r) & \cos(\tilde{\theta}_r) \end{bmatrix} \cdot \begin{bmatrix} x_d^r \\ x_q^r \end{bmatrix} \\ &= \mathbf{R}(\tilde{\theta}_r) \cdot \mathbf{x}_{dq}^r \end{aligned} \quad (8)$$

where x stands for an arbitrary variable, e.g., current, voltage, flux linkage, etc. Superscripts "r," "̂r," and "s" represent RRF, ERRF, and stationary reference frame, respectively. Then, the

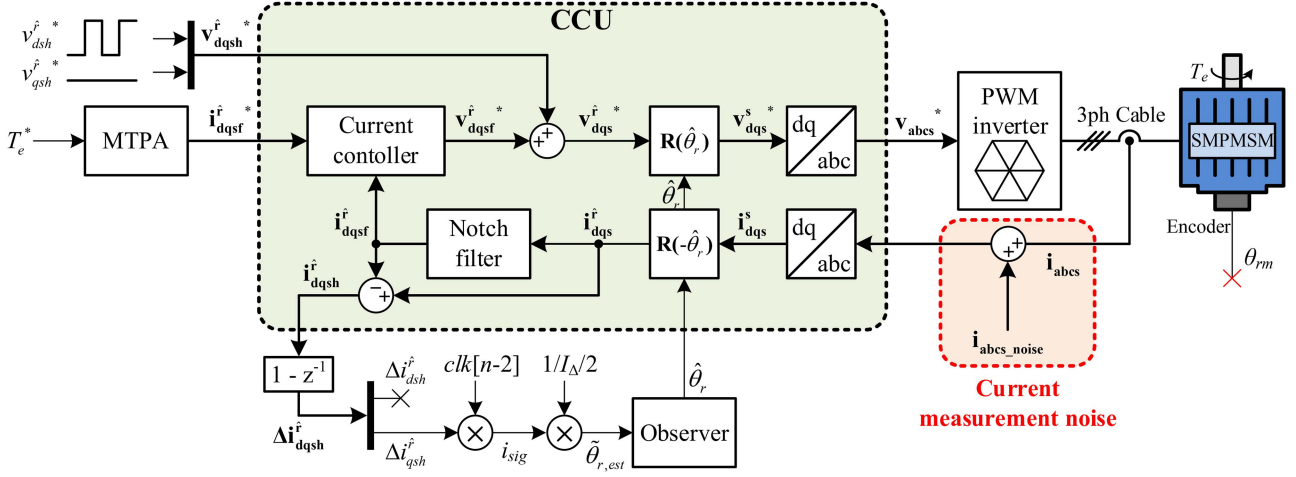


Fig. 15. Block diagram of square wave-injection sensorless drive system.

voltage reference of the SISC algorithm can be divided into two parts, as shown in Fig. 15, i.e., \hat{v}_{dqs}^* is the sum of \hat{v}_{dqsf}^* and \hat{v}_{dqsh}^* . Superscript “*” stands for the reference variables. Subscript “*f*” means the fundamental frequency components and “*h*” means the injection (high) frequency components. \hat{v}_{dqs}^* is transformed into the three-phase voltage reference, \hat{v}_{abcs}^* , and it is synthesized by the PWM inverter.

The SISC is generally used in the low-speed operation, so the two frequencies are fully apart from each other. Then, \hat{v}_{dqsf}^* and \hat{v}_{dqsh}^* are the output of the current controller and the injected voltage, respectively. \hat{v}_{dqsh}^* adopted in this article is expressed as a square wave as

$$\hat{v}_{dqsh}^*[n] = \begin{bmatrix} V_h \\ 0 \end{bmatrix} \cdot \text{clk}[n] \quad (9)$$

where V_h is the magnitude of the injection voltage and $\text{clk}[n]$ is a clock signal alternating between +1 and -1 in the injection frequency (F_{inj}). The voltage is injected to the estimated *d*-axis to mitigate the torque ripple induced by the voltage injection. The voltage reference generated in *n*th sample is synthesized by the inverter between *n*+1th sample and *n*+2th sample. Then, the current response according to the injection voltage can be represented in RRF with the dq-dynamic inductances as

$$\hat{v}_{dqsh}^*[n] = \frac{1}{T_s} \begin{bmatrix} L_{dh} & L_{dqh} \\ L_{qdh} & L_{qh} \end{bmatrix} \cdot \Delta i_{dqsh}^*[n+2] \quad (10)$$

where $\Delta i_{dqsh}^*[n+2] = i_{dqsh}^*[n+2] - i_{dqsh}^*[n+1]$ and T_s is the sampling period. The meaning of $\Delta i_{dqsh}^*/T_s$ is differentiation. The three-phase current, i_{abcs} , is measured and transformed into ERF current vector, \hat{i}_{dqs} . By the notch filter in Fig. 15, the measured current is divided into two frequency terms, \hat{i}_{dqsf} and \hat{i}_{dqsh} , which are used for the fundamental current control and the rotor position estimation, respectively.

The *q*-axis current response on ERF is demodulated into a signal, i_{sig} , with a simple multiplication as

$$i_{\text{sig}}[n] \triangleq \Delta i_{qsh}^*[n] \cdot \text{clk}[n-2]. \quad (11)$$

By combining (8)~(11), i_{sig} can be revealed as

$$i_{\text{sig}}[n] = I_\Delta \cdot \sin(2\tilde{\theta}_r - 2\phi_\Delta) \quad (12)$$

where $I_\Delta = \frac{V_h T_s \sqrt{L_{dqs}^2 + \Delta L_h^2}}{L_{dh} L_{qh} - L_{dqs}^2}$, $\phi_\Delta = \frac{1}{2} \text{atan}2(L_{dqs}, -\Delta L_h)$, and $\Delta L_h \triangleq \frac{L_{dh} - L_{qh}}{2}$. Then, the estimated value of $\tilde{\theta}_r$ can be calculated with i_{sig} as

$$\tilde{\theta}_{r,\text{est}}[n] = \frac{1}{2} \cdot \frac{i_{\text{sig}}[n]}{I_\Delta} = \frac{1}{2} \cdot \sin(2\tilde{\theta}_r - 2\phi_\Delta) \approx \tilde{\theta}_r - \phi_\Delta. \quad (13)$$

The third term can be approximated to the fourth term, when $\tilde{\theta}_r - \phi_\Delta$ is close to zero. $\tilde{\theta}_{r,\text{est}}$ is used as the input of the proportional-integral-differential (PID) type position observer [22], [23], as shown in Fig. 15. The outputs of the observer are the estimated rotor angle, $\hat{\theta}_r$, and the estimated rotor speed, $\hat{\omega}_r$. The observer makes $\hat{\theta}_r$ converge into a certain angle, where $\hat{\theta}_{r,\text{est}}$ becomes null. As a result, $\hat{\theta}_r$ becomes equal to ϕ_Δ , which is usually close to zero. If $\tilde{\theta}_r$ becomes zero, $\hat{\theta}_r$ would be identical to θ_r .

Next, the SISC simulation considering the current measurement noise is implemented with a six pole IPMSM. For the static inductances, $L_{ds} = 7.13$ mH, $L_{qs} = 11.04$ mH, $L_{dqs} = 0$ mH. The permanent magnet flux linkage, $\lambda_f = 62.5$ mWb · t, and the stator resistance, $R_s = 0.8$ Ω. The peak value of the rated current is 4.08 A. The spatial harmonics and the magnetic saturation of the motor are not considered in the simulation. Therefore, the dynamic inductances are the same with the static inductances. As a result, L_{dqh} is nullified and ϕ_Δ is calculated as zero by its definition.

For the inverter side parameters, V_{dc} is 150 V and switching frequency (F_{sw}) is 10 kHz. F_{inj} is set as a half of F_{sw} , which is one of the commonly used injection frequencies for the SISC operation [7], [8], [11], [15], [23]. V_h is set as 20 V, which is 13.33% of V_{dc} . Double sampling per a switching period is adopted, i.e., the sampling event occurs in every peak and valley of the triangle carrier wave for PWM [21]. The inverter nonlinearity and the three-phase asymmetry are not considered in the simulation.

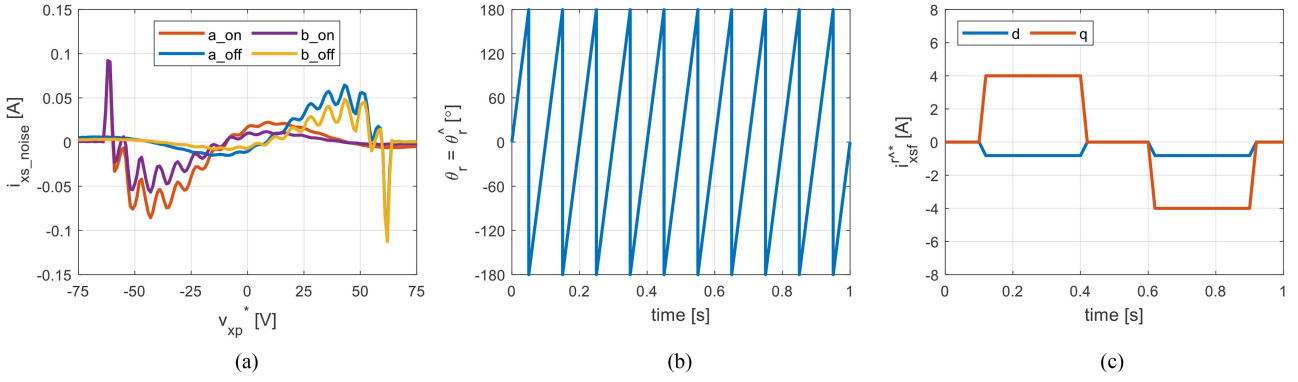


Fig. 16. (a) Sampled current measurement noise of “a” and “b” phases. (b) Rotating θ_r and $\hat{\theta}_r$. (c) Smoothly varying i_{dqsf}^{r*} .

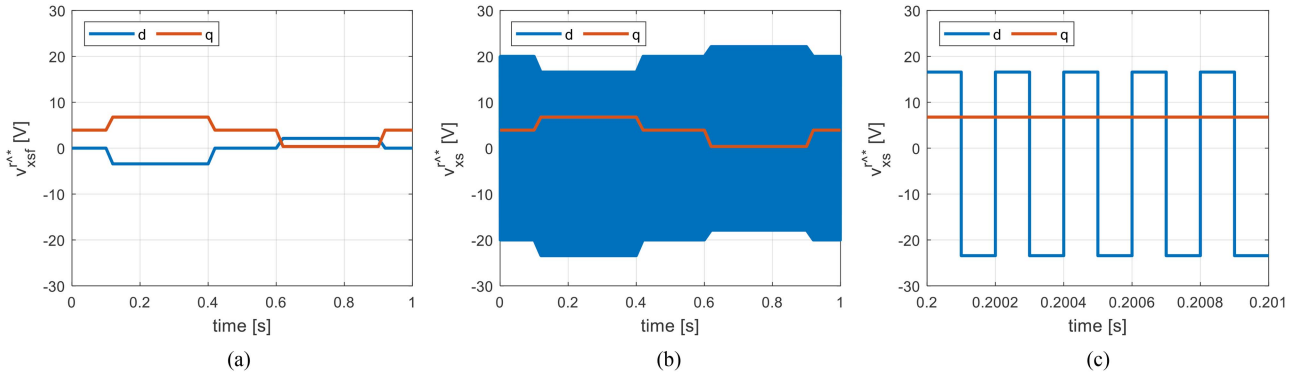


Fig. 17. (a) v_{dqsf}^{r*} , (b) v_{dqs}^{r*} , and (c) close-up of v_{dqs}^{r*} .

At the output terminal of the three-phase inverter, only two current sensors are installed in “a” and “b” phases. The current measurement noise graphs, used in the simulation, are provided in Fig. 16(a). They are experimentally sampled from the current sensors, which are used in the experiments, described later. A manufacturing tolerance appears between the two sensors. Then, “c” phase current is calculated from the other two phase currents, under the assumption of $i_{cs} = -i_{as} - i_{bs}$.

For the operating conditions, the rotating speed is 200 r/min, where $\omega_r = 10$ Hz. The PID type position observer is deactivated and $\hat{\theta}_r$ is manually synchronized with θ_r , as shown in Fig. 16(b), i.e., $\hat{\theta}_r = 0$. The high-frequency voltage is exactly injected to the real d -axis. As a result, $\theta_{r,est}$ in (13) should be computed as null in steady states, since ϕ_Δ is set as zero. However, the only considered disturbance factor, the current measurement noise, makes $\hat{\theta}_{r,est}$ have nonzero signal.

In the simulation, the torque command is smoothly varying from $0 \rightarrow 1 \rightarrow 0 \rightarrow -1 \rightarrow 0$ per unit (pu) of the rated torque. i_{dqsf}^{r*} accordingly changes as Fig. 16(c). In the steady states, the required fundamental frequency voltage reference on ERFF can be calculated as

$$\begin{bmatrix} v_{dsf}^{r*} \\ v_{qsf}^{r*} \end{bmatrix} = R_s \begin{bmatrix} i_{dsf}^{r*} \\ i_{qsf}^{r*} \end{bmatrix} + \omega_r \begin{bmatrix} 0 & -1 \\ 1 & 0 \end{bmatrix} \cdot \left\{ \begin{bmatrix} L_{ds} i_{dsf}^{r*} \\ L_{qs} i_{qsf}^{r*} \end{bmatrix} + \begin{bmatrix} \lambda_f \\ 0 \end{bmatrix} \right\}. \quad (14)$$

The result is represented in Fig. 17(a). The injection voltage, v_{dqsf}^{r*} , is added on v_{dqsf}^{r*} in Fig. 17(b). The close-up waveform of ten switching periods is given in Fig. 17(c). As $F_{inj} = F_{sw}/2$, d -axis voltage reference alternates five times in the close-up figure. Then, v_{dqs}^{r*} can be transformed into the three-phase voltage reference with $\hat{\theta}_r$ in Fig. 16(b). The result is Fig. 18(a). By substituting the three-phase voltage reference into Fig. 16(a), the current measurement noise of the three-phase can be calculated as Fig. 18(b). As aforementioned, i_{cs_noise} is calculated from i_{as_noise} and i_{bs_noise} .

The signal processing of the SISC is implemented with the sampled noise of Fig. 18(b). The sampled noise, i_{abcs_noise} , is added to i_{abcs} with the superposition rule. It can be represented in the block diagram of the SISC, as Fig. 15. The $\hat{\theta}_{r,est}$ signal induced from the noise is calculated as Fig. 19(a). As shown in Fig. 16(c), the torque reference is maintained as 1 pu at $0.2 \sim 0.3$ second, 0 pu at $0.45 \sim 0.55$ second, and -1 pu at $0.7 \sim 0.8$ second. The time intervals are 0.1 second, which is the same with one period of the rotating frequency, 10 Hz. Then, the DFT results of the $\hat{\theta}_{r,est}$ signal at the three time intervals are depicted in Fig. 19(b). It can be observed in Fig. 19 that a considerable amount of $\hat{\theta}_{r,est}$ is induced from the current measurement noise, regardless of the current operating points.

Then, the same waveform is obtained with an experiment. The nominal parameters of the target motor are the same with the

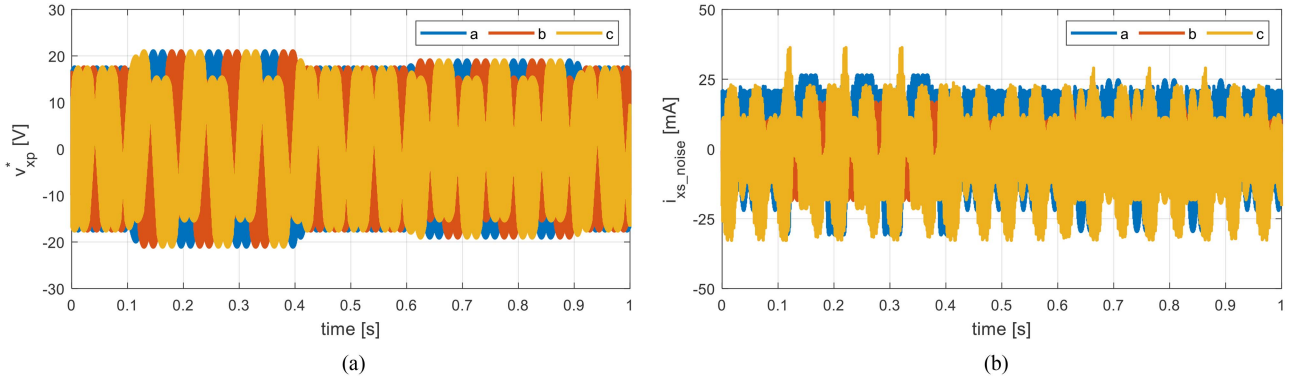
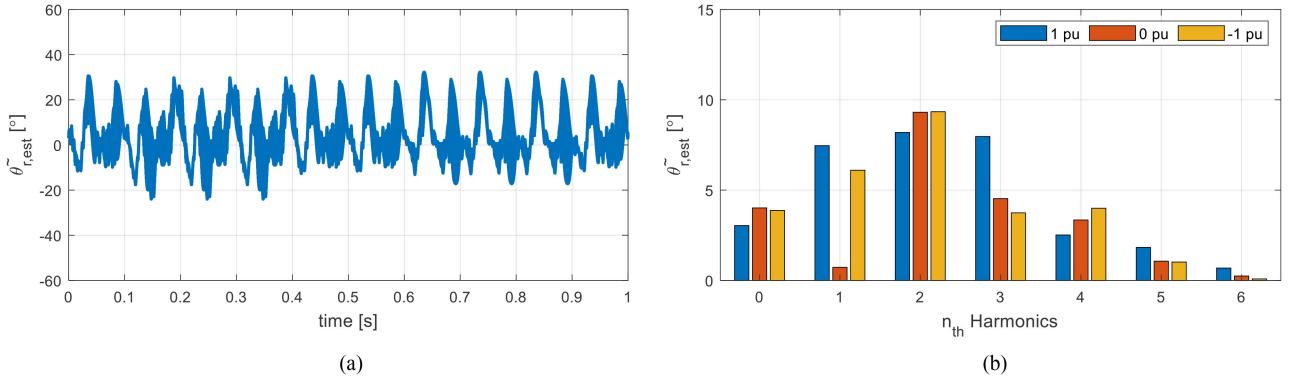
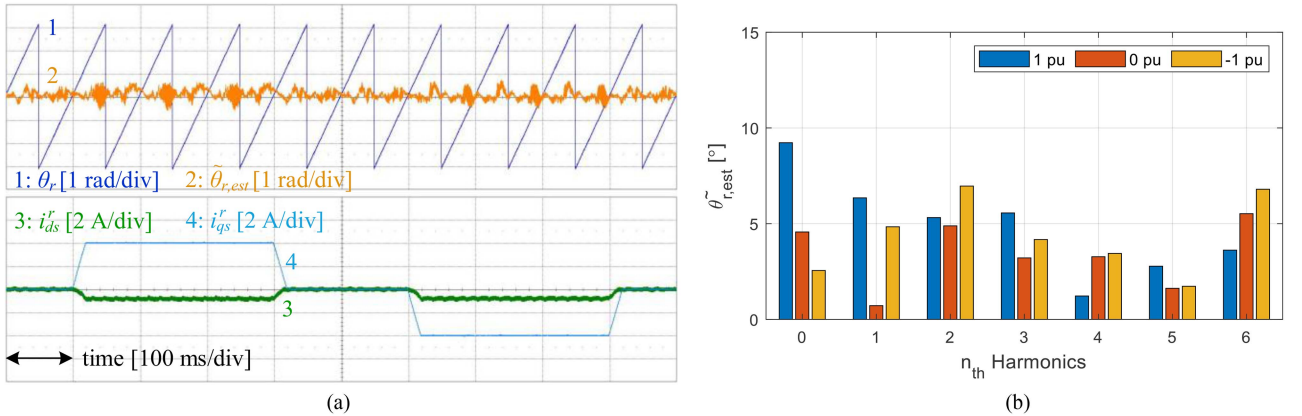


Fig. 18. (a) Three-phase voltage reference. (b) Three-phase current measurement noise.

Fig. 19. (a) $\tilde{\theta}_{r,est}$ induced by current measurement noise. (b) DFT results. (Simulation).Fig. 20. (a) $\tilde{\theta}_{r,est}$ induced by current measurement noise. (b) DFT results. (Experiment).

simulation, but cross-coupling inductance, magnetic saturation, and spatial harmonics exist in the actual machine. The inverter and the SISC parameters also follow the simulation, but there is undesirable inverter nonlinearity. The rotating speed is rigidly controlled by the load machine as 200 r/min and θ_r is obtained from a high-resolution encoder system. As aforementioned, the PID type position observer is deactivated and $\tilde{\theta}_r$ is manually synchronized with θ_r . With the conditions, the $\tilde{\theta}_{r,est}$ signal is obtained by the signal processing and represented in Fig. 20(a).

The DFT results are depicted in Fig. 20(b). In the comparison of Figs. 19 and 20, the $\tilde{\theta}_{r,est}$ signals in the two figures are similar to each other. Slight differences come from the disturbance factors [5], [6], [7], [8], [9], [10], [11], [12], [13], [14], [15], [16], [17], [18], which are not considered in the simulation. For example, the difference in 6th harmonic frequency is prominent, and it comes from the spatial harmonics of the target motor [7], [15]. In [15], the 2nd, 3rd, and 6th harmonics of position estimation error are matched with their dominant disturbance

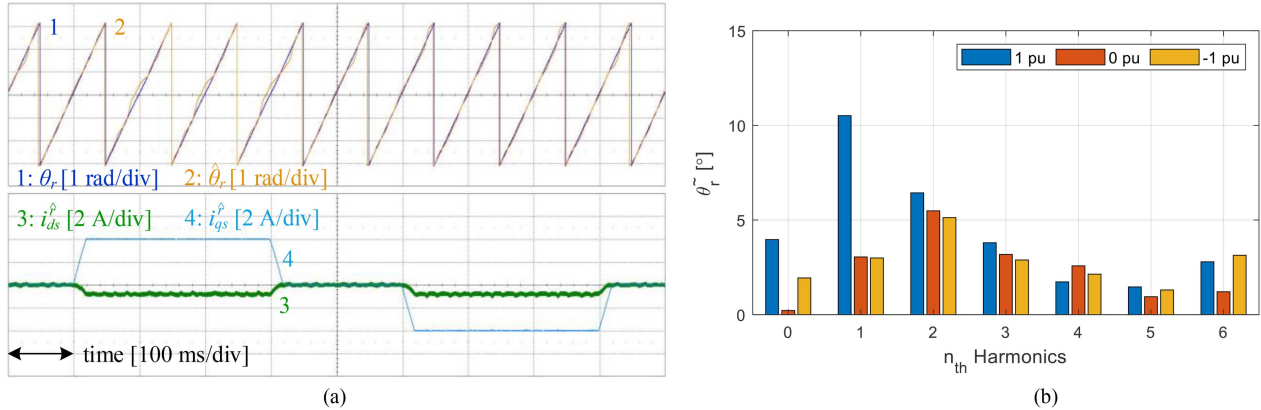


Fig. 21. (a) Position estimation with SISC operation. (b) DFT results of $\tilde{\theta}_r$. (Experiment).

factors, respectively; 2nd harmonic for three-phase asymmetry and scale error of current sensors, 3rd harmonic for inverter nonlinearity, and 6th harmonic for spatial harmonics of a target motor. However, as shown in Fig. 19(b), the position estimation error caused by the current measurement noise would spread over many harmonic frequencies; not a certain frequency is dominant. Furthermore, it can be expected in the comparison of Figs. 19(b) and 20(b) that a significant portion of the $\tilde{\theta}_{r,est}$ signal is induced from the current measurement noise.

The full operation of the SISC is implemented with a disconnected encoder system and activated PID type position observer, i.e., $\tilde{\theta}_{r,est}$ is used for the position estimation. Then, $\tilde{\theta}_r$ is shown in Fig. 21(a) and DFT results of the $\tilde{\theta}_r$ signal is represented in Fig. 21(b). As shown in the figures, it is verified that the current measurement noise severely downgrades the SISC performance.

In this article, only the SISC with $F_{inj} = F_{sw}/2$ is exemplified to analyze the noise effects on the position estimation. Similarly, for other injection frequencies, i.e., $F_{inj} \neq F_{sw}/2$, the current measurement noise would also deteriorate the SISC performance. When the injection voltage level is fixed, the magnitude of the induced current response is inversely proportional to the injection frequency. In accordance with signal-to-noise ratio (SNR), the sensorless control could be more robust against the current measurement noise with the decreased injection frequency, because the current response becomes larger, and it results in the increased SNR. Otherwise, when the generally used switching frequency grows up with SiC or GaN devices, sensorless control with the “half-switching” or “switching” frequency signal-injection could become more vulnerable to the current measurement noise.

VI. CONCLUSION

This article specifically analyzes the noise-inducing mechanism of CHCSs, induced from the inverter dv/dt . In the analysis, it is revealed that leakage current flows through the parasitic capacitances between the inverter and the sensor, and it results in the current measurement noise. Many experimental results are suggested to support the analysis. Several CHCSs from different manufacturers, which have the same measurement range, are additionally tested to generalize the description. The noise is

sampled with ADC circuits and it is newly defined as a function of the pole voltage reference. Because the signal processing for the SISC is progressed based on the sampled current, which is contaminated by the noise, there is an inevitable estimation error and it is precisely predicted with the proposed theory. The effectiveness of the proposed theory is verified by the comparison of the simulation and experimental results. Consequently, it has been figured out that a considerable position estimation error occurs in the SISC operation with the CHCSs and the inverter system.

REFERENCES

- [1] N. Bianchi and S. Bolognani, “Influence of rotor geometry of an IPM motor on sensorless control feasibility,” *IEEE Trans. Ind. Appl.*, vol. 43, no. 1, pp. 87–96, Jan./Feb. 2007.
- [2] J. Jang, S. Sul, J. Ha, K. Ide, and M. Sawamura, “Sensorless drive of surface-mounted permanent-magnet motor by high-frequency signal injection based on magnetic saliency,” *IEEE Trans. Ind. Appl.*, vol. 39, no. 4, pp. 1031–1039, Jul./Aug. 2003.
- [3] T. Aihara, A. Toba, T. Yanase, A. Mashimo, and K. Endo, “Sensorless torque control of salient-pole synchronous motor at zero-speed operation,” *IEEE Trans. Power Electron.*, vol. 14, no. 1, pp. 202–208, Jan. 1999.
- [4] Z. Chen, X. Cai, R. Kennel, and F. Wang, “Enhanced sensorless control of SPMSM based on stationary reference frame high-frequency pulsating signal injection,” in *Proc. Int. Power Electron. Motion Control Conf.*, 2016, pp. 885–890.
- [5] Z. Zhu, Y. Li, D. Howe, and C. Bingham, “Compensation for rotor position estimation error due to cross-coupling magnetic saturation in signal injection based sensorless control of PM brushless AC motors,” in *Proc. IEEE Int. Electric Mach. Drives Conf.*, 2007, pp. 208–213.
- [6] Y. Li, Z. Zhu, D. Howe, C. Bingham, and D. Stone, “Improved rotor-position estimation by signal injection in brushless AC motors, accounting for cross-coupling magnetic saturation,” *IEEE Trans. Ind. Appl.*, vol. 45, no. 5, pp. 1843–1850, Sep./Oct. 2009.
- [7] Y. Kwon, J. Lee, and S. Sul, “Extending operational limit of IPMSM in signal-injection sensorless control by manipulation of convergence point,” *IEEE Trans. Ind. Appl.*, vol. 55, no. 2, pp. 1574–1586, Mar./Apr. 2019.
- [8] Y. Lee, Y. Kwon, and S. K. Sul, “Realization of signal-injection sensorless control of SMPMSM by modification of current trajectory,” in *Proc. IEEE Energy Convers. Congr. Expo.*, 2020, pp. 5117–5123.
- [9] G. Bi, G. Zhang, G. Wang, Q. Wang, Y. Hu, and D. Xu, “Adaptive iterative learning control based rotor position harmonic error suppression method for sensorless PMSM drives,” *IEEE Trans. Ind. Electron.*, vol. 69, no. 11, pp. 10870–10881, Nov. 2022.
- [10] G. Zhang, G. Wang, D. Xu, and N. Zhao, “ADALINE-Network-Based PLL for position sensorless interior permanent magnet synchronous motor drives,” *IEEE Trans. Power Electron.*, vol. 31, no. 2, pp. 1450–1460, Feb. 2016.

- [11] Y. Kwon and S. Sul, "Reduction of injection voltage in signal injection sensorless drives using a capacitor-integrated inverter," *IEEE Trans. Power Electron.*, vol. 32, no. 8, pp. 6261–6274, Aug. 2017.
- [12] Y. Lee, Y. Kwon, and S. Sul, "Improved signal-injection sensorless control robust to inverter nonlinearity effects by prediction of voltage disturbance," in *Proc. IEEE Transp. Electricr. Conf. Expo.*, 2019, pp. 1–5.
- [13] R. Raute, C. Caruana, C. Staines, J. Cilia, M. Sumner, and G. Asher, "Analysis and compensation of inverter nonlinearity effect on a sensorless PMSM drive at very low and zero speed operation," *IEEE Trans. Ind. Electron.*, vol. 57, no. 12, pp. 4065–4074, Dec. 2010.
- [14] J. Guerrero, M. Leetmaa, F. Briz, A. Zamarron, and R. Lorenz, "Inverter nonlinearity effects in high-frequency signal-injection-based sensorless control methods," *IEEE Trans. Ind. Appl.*, vol. 41, no. 2, pp. 618–626, Mar./Apr. 2005.
- [15] C. Hwang, Y. Lee, and S. Sul, "Analysis on position estimation error in position-sensorless operation of IPMSM using pulsating square wave signal injection," *IEEE Trans. Ind. Appl.*, vol. 55, no. 1, pp. 458–470, Jan./Feb. 2019.
- [16] P. Xu and Z. Zhu, "Carrier signal injection-based sensorless control for permanent-magnet synchronous machine drives considering machine parameter asymmetry," *IEEE Trans. Ind. Electron.*, vol. 63, no. 5, pp. 2813–2824, May 2016.
- [17] D. Chung and S. Sul, "Analysis and compensation of current measurement error in vector controlled AC motor drives," *IEEE Trans. Ind. Appl.*, vol. 34, no. 2, pp. 340–345, Mar./Apr. 1998.
- [18] M. Harke, J. Guerrero, M. Degner, F. Briz, and R. Lorenz, "Current measurement gain tuning using high-frequency signal injection," *IEEE Trans. Ind. Appl.*, vol. 44, no. 5, pp. 1578–1586, Sep./Oct. 2008.
- [19] E. Ramsden, *Hall-Effect Sensors: Theory and Application*. Amsterdam, The Netherlands: Elsevier, 2011, pp. 1–10.
- [20] F. Li, X. Luo, X. Cheng, and S. Liu, "Impact of the winding area of enameled wire on packaging performance of a closed loop Hall effect current sensor," in *Proc. IEEE Electron. Compon. Technol. Conf.*, 2012, pp. 1631–1635.
- [21] H. Wang, M. Yang, L. Niu, and D. Xu, "Current-loop bandwidth expansion strategy for permanent magnet synchronous motor drives," in *Proc. IEEE Conf. Ind. Electron. Appl.*, 2010, pp. 1340–1345.
- [22] R. Lorenz and K. Patten, "High-resolution velocity estimation for all-digital, AC servo drives," *IEEE Trans. Ind. Appl.*, vol. 27, no. 4, pp. 701–705, Jul./Aug. 1991.
- [23] D. Kim, Y. Kwon, S. Sul, J. Kim, and R. Yu, "Suppression of injection voltage disturbance for high-frequency square-wave injection sensorless drive with regulation of induced high-frequency current ripple," *IEEE Trans. Ind. Appl.*, vol. 52, no. 1, pp. 302–312, Jan./Feb. 2016.
- [24] A. Consoli, G. Bottiglieri, G. Scarella, and G. Scelba, "Flux and voltage calculations of induction motors supplied by low- and high-frequency currents," *IEEE Trans. Ind. Appl.*, vol. 45, no. 2, pp. 737–746, Mar./Apr. 2009.
- [25] J. Ha and S. Sul, "Sensorless field-orientation control of an induction machine by high-frequency signal injection," *IEEE Trans. Ind. Appl.*, vol. 35, no. 1, pp. 45–51, Jan./Feb. 1999.
- [26] F. Briz, M. Degner, J. Guerrero, A. Zamarron, and R. Lorenz, "Implementation issues affecting the performance of carrier signal injection based sensorless controlled AC drives," in *Proc. Conf. 36th IAS Annu. Meeting IEEE Ind. Appl.*, 2001, vol. 4, pp. 2645–2652.
- [27] P. Garcia, F. Briz, M. Degner, and D. Diaz-Reigosa, "Accuracy, bandwidth, and stability limits of carrier-signal-injection-based sensorless control methods," *IEEE Trans. Ind. Appl.*, vol. 43, no. 4, pp. 990–1000, Jul./Aug. 2007.



Yoon-Ro Lee (Member, IEEE) was born in Anyang, South Korea, in 1992. He received the B.S., M.S., and Ph.D. degrees in electrical engineering and computer science from Seoul National University, Seoul, South Korea, in 2015, 2017, and 2021, respectively.

He is currently a Senior Engineer with Rivian Automotive LLC, Carson, CA, USA. His research interests include the control of electric vehicles, electrical machines, and power conversion systems with power electronics.



Jiwon Yoo (Member, IEEE) was born in Seoul, South Korea in 1990. He received the B.S. and Ph.D. degrees in electrical and computer engineering from Seoul National University, Seoul, South Korea, in 2017 and 2022, respectively.

From 2014 to 2017, he was a Research Engineer with Seoho Electric Company, Anyang, South Korea. His research interests include power electronics, control of electric machines, power semiconductors, and sensorless drives.

He was the recipient of the Best Paper Award First Prize at 2019 International Conference on Power Electronics (ICPE-Busan/ECCE-Asia) and the Best Paper Award at 2020 International Power Electronics and Motion Control Conference (IPEMC-Nanjing/ECCE-Asia).



Inhwi Hwang (Member, IEEE) was born in Seoul, South Korea, in 1996. He received the B.S. and M.S. degrees in electrical engineering from Seoul National University, Seoul, South Korea, in 2020 and 2022, respectively.

His research interests include control of electric machines, converters, and power semiconductor physics.



Seung-Ki Sul (Fellow, IEEE) received the B.S., M.S., and Ph.D. degrees in electrical engineering from Seoul National University, Seoul, Korea, in 1980, 1983, and 1986, respectively.

His research interests include control of electrical machines, electric/hybrid vehicles, electric propulsion of ship, and power conditioning system for renewables.

Since 1991, he has been a Member of faculty of School of the Electrical and Computer Engineering, Seoul National University, where he is currently a Professor. Since year 2000, he has been an IEEE Fellow. He has authored or coauthored more than 140 IEEE reviewed journal papers and more than 340 international conference papers in the area of power electronics. For a year of 2015, he was the president of Korea Institute of Power Electronics. He was the recipient of the Outstanding Achievement Award from IEEE IAS in 2016 and the William E Newell award from IEEE PELS in this year.